

Spin-Valley Locking Effect in Defect States of Monolayer MoS₂

Yaqian Wang^{1,2}, Longjiang Deng^{1,2}, Qilin Wei³, Yi Wan⁴, Zhen Liu^{1,2}, Xiao Lu^{1,2}, Yue Li^{1,2}, Lei Bi^{1,2}, Li Zhang^{1,2}, Haipeng Lu^{1,2}, Haiyan Chen^{1,2}, Peiheng Zhou^{1,2}, Linbo Zhang^{1,2}, Yingchun Cheng^{3,*}, Xiaoxu Zhao^{5,*}, Yu Ye⁴, Wei Huang³, Stephen John Pennycook⁵, Kian Ping Loh⁶ and Bo Peng^{1,2,*}

¹ National Engineering Research Center of Electromagnetic Radiation Control

Materials, School of Electronic Science and Engineering, University of Electronic Science and Technology of China, Chengdu, 611731, China

² State Key Laboratory of Electronic Thin Films and Integrated Devices, University of Electronic Science and Technology of China, Chengdu, 611731, China

³ Key Laboratory of Flexible Electronics & Institute of Advanced Materials, Nanjing Tech University, Nanjing, 211816, China

⁴ State Key Laboratory for Artificial Microstructure & Mesoscopic Physics, Frontiers Center for Nano-optoelectronics, School of Physics, Peking University, Beijing 100871, China

⁵ Department of Materials Science and Engineering, National University of Singapore, 9 Engineering Drive 1, 117575, Singapore

⁶ Department of Chemistry and Centre for Advanced 2D Materials and Graphene Research Centre, National University of Singapore, 117549, Singapore

* To whom correspondence should be addressed. Email address:

bo_peng@uestc.edu.cn (B.P.); iamyccheng@njtech.edu.cn (Y.C.C);

xiaoxu_zhao@u.nus.edu (X.X.Z)

Abstract: Valley pseudospin in two-dimensional (2D) transition-metal dichalcogenides (TMDs) allows optical control of spin-valley polarization and intervalley quantum coherence. Defect states in TMDs give rise to new exciton features and theoretically exhibit spin-valley polarization; however, experimental achievement of this phenomenon remains challenges. Here, we report unambiguous valley pseudospin of defect-bound localized excitons in CVD-grown monolayer MoS₂; enhanced valley Zeeman splitting with an effective g -factor of -6.2 is observed. Our results reveal that all five d -orbitals and the increased effective electron mass contribute to the band shift of defect states, demonstrating a new physics of the magnetic responses of defect-bound localized excitons, strikingly different from that of A excitons. Our work paves the way for the manipulation of the spin-valley degrees of freedom through defects toward valleytronic devices.

Keywords: valleytronic, spintronic, spin manipulation, defect engineering, defect exciton

Manipulation of the spin degree of freedom (DOF) at the atomic scale is crucial in exploring new spintronic and valleytronic devices for quantum information and communication technologies.¹⁻⁶ Defects originating from zigzag edge, dislocations and deformations have been experimentally and theoretically demonstrated to lead to long-range magnetic order in transition-metal dichalcogenides (TMDs);⁷⁻¹⁰ the proton irradiation induce vacancy defects in MoS₂ bulk, giving rise to ferromagnetism.¹¹ Theoretical studies have also predicted that magnetic atom substitutional doping can introduce magnetic ordering in TMDs;¹²⁻¹⁵ and recent experimental works have demonstrated that Zeeman splitting of valley pseudospin is enhanced by Co and Fe atom doping in MoS₂ monolayer.¹⁶⁻¹⁷ These create opportunities for spin control and manipulation in TMDs by defects. In parenthesis, defects in 2D materials can more strongly trap free carriers and localize excitons and influence their physical properties, opening up plenty of opportunities to tailor the transport and optical properties of 2D materials. Dopant defects modify the electronic structures of monolayer TMDs, resulting in a shift in the PL peak energy;¹⁸ vacancy defects induce a new low-energy suboptical gap inside the bandgap and lead to a sub-bandgap emission from defect-bound localized excitons.¹⁹⁻²⁰ Single photon emission in two-dimensional materials due to single defect²¹⁻²⁵ and nanoscale strain,²⁶⁻²⁷ particularly in monolayer WSe₂ and BN,²⁸⁻³³ have also been demonstrated.

Coupling of the broken spatial inversion symmetry and strong spin-orbit coupling (SOC) leads to valley pseudospin in monolayer TMDs, in which spin-up holes and spin-down electrons reside in the +K and -K valleys.³⁴ The separated valleys in

momentum space can be regarded as a unique DOF for information coding and transmission. Most recently, spin-valley polarization of defect states in monolayer TMDs has been theoretically predicted.^{19, 35} The presence of defects in monolayer TMDs leads to quenching of the circularly polarized photoluminescence (PL) emission of A and B excitons and degradation of their valley polarization due to the increased nonradiative decay rate.³⁶ Magnetic field can break the valley degeneracy and tune the valley polarization of defect states.³⁷ Although the emission of defect-bound excitons attributed to chalcogen vacancies has been studied in monolayer MoS₂, MoSe₂, WS₂ and WSe₂.^{20, 38-41} However, to date, experimentally manipulating the valley pseudospin and splitting of defect states still remains challenging.

In this work, we report observation of valley pseudospin of defect-bound excitons in CVD-grown monolayer MoS₂ by circularly polarized PL spectroscopy; a strong polarization-resolved defect emission is observed at 10 K. Remarkably, the valley pseudospin of defect states can be lifted by a magnetic field, analogous to valley Zeeman splitting of intrinsic A excitons of monolayer MoS₂, giving an effective g -factor of approximately -6.2, which is consistent with the theoretical g -factor of -6.6. We proposed that the valley pseudospin and valley Zeeman splitting of defect excitons originate from the momentum-dependent carrier distribution of defect states in the vicinity of $\pm K$ valleys; the enhanced g -factor arises from the increased effective electron mass and d -orbital magnetic moment.

Monolayer MoS₂ belongs to the nonsymmorphic space group (D_{6h}^4 symmetry and

$P6_3/mmc$ space group). In each unit cell, one Mo atom is coordinated by six S atoms and sandwiched between S atoms, forming a S-Mo-S trigonal prismatic geometry, which further shares vertexes to build a hexagonal closed-packed network (Fig. 1a and b). We studied the electronic band structures of monolayer MoS₂ in the presence of with one single S vacancy (V_S) and S divacancy (V_{2S}) by first-principles calculations.⁴²⁻⁴³ Pristine monolayer MoS₂ without any defect exhibits a distinguishable carrier distribution in two momentum-dependent valleys; spin-up holes and spin-down electrons are only kept in the valence and conduction band edge in the +K and -K valleys (Supplementary Information Fig. S1c).^{2-3,34} Importantly, the defect states also have a unique electronic band structure with two momentum-dependent band minima at the +K and -K points of the Brillouin zone (Fig. 1c). The defect band edges of both the V_S and V_{2S} have spin-up and spin-down states in the +K and -K valleys, respectively, while the valence band edges show opposite spin states in the same valley with defect states, suggesting valley pseudospin of defect states and distinct momentum-dependent carrier distribution (Fig. 1d and Supplementary Information Fig. S1).

Structural defects can be produced in TMDs through the CVD method, such as grain boundaries, various vacancy defects and substitutional defects.⁴⁴⁻⁴⁵ Moreover, chalcogenide vacancies easily form due to their low formation energy and the high volatility of chalcogenides.¹⁵ Therefore, we designed experimental conditions to grow defect-engineered monolayer MoS₂ on Si/SiO₂ substrates by the CVD method (See Methods).⁴⁶ The Raman frequency difference between the E_{2g} and A_{1g} modes is ~20

cm^{-1} (See Supplementary Information Fig. S2), which satisfies the criteria of CVD-grown monolayer MoS_2 on SiO_2/Si substrates.⁴⁷ To validate the S vacancies, we investigated the structure of the CVD-grown monolayer MoS_2 on an atomic scale by employing an aberration-corrected scanning transmission electron microscope with an annular dark field detector (STEM-ADF) operated at low accelerating voltage (60 kV). The maximum transferred energy from 60 kV electron beam is lower than the threshold of the knock on damage of MoS_2 , thus the defects cannot be induced by electron beam. From the top view, monolayer MoS_2 is a hexagonal closed-packed structure; one Mo atom is surrounded by three S atoms, and *vice versa*. Only V_S and V_{2S} defects are observed. The location and density of V_S and V_{2S} is reflected by the contrast reduction in the STEM-ADF image. The mapping of all atom species of the MoS_2 monolayer is depicted in Fig. 2a. Selected V_{2S} are highlighted by white dashed circle. Numerous V_S and V_{2S} defects are unambiguously observed. The distributions of V_S (white spheres) and V_{2S} (yellow spheres) defects were shown in corresponding atomic mode (Fig. 2a). Enlarged STEM-ADF images clearly show that two edge-shared top and bottom S atoms in 1H- MoS_2 triangular prism escape simultaneously in V_{2S} , while only one S atom run away in V_S (Fig. 2b), consistent with corresponding simulated images.

Figure 2c and d show the temperature dependence of the PL spectra upon excitation by light at 2.41 eV. The PL emissions of the A exciton (X^A) are blueshifted due to the crystal lattice contraction as the temperature decreases.⁴⁸ Above 150 K, PL emissions of A excitons are strikingly observed, and a new PL peak (X^D) appears under further

cooling, which overlaps with the A exciton PL peak with similar PL intensity, thus resulting in broadened line widths in the region of 150-75 K (Fig. 2d). However, the PL intensity of the A exciton drastically decreases below 75 K; the strong emission X^D at ~ 1.74 eV is unambiguously observed, which has a Stokes shift of ~ 0.14 eV and an over twofold enhancement in the PL intensity as compared to the A exciton at 10 K. Figure 2e shows the absorption spectra of monolayer MoS₂ at 10 K. The A and B exciton absorption features are distinct; however, a new absorption feature at approximately 1.74 eV is strikingly detected. The splitting between the X^A and X^D is approximately 0.14 eV, similar to the PL emission spectra. The optically excited electron-hole pairs can be bound to excessive electrons by Coulomb interactions in the heavily doped sample, giving rise to charged excitons (trions or Fermi polarons) in different doping regimes, leading to a PL emission below X^A , however, the Stokes shifts of trion and polarons should be ~ 40 meV,^{4, 49-51} which is much smaller than that of X^A and X^D in our MoS₂. Therefore, the possibility of trions is ruled out. The strong emissions X^D are attributed to the defect-bound excitons induced by chalcogen vacancies,^{20, 37, 52} rather than charged excitons. The first-principles calculation results in Fig. 1d show that the defect states arising from S vacancy in monolayer MoS₂ appear at ~ 0.55 eV below the conduction band minimum (CBM), which is in agreement with the reported predicted results (~ 0.6 eV).⁵³⁻⁵⁴ The band gap between defect states and CBM consists of the binding energy of A exciton and Stokes energy shift between the X^A and X^D . Thus, the binding energy of X^A is estimated to be approximately 0.41 eV, which is also consistent with the reported experimental

results,⁵⁵⁻⁵⁶ indicating that our calculated results of S vacancy defects are consistent with the experimental STEM-ADF and PL results.

The defect emission is still striking under nearly on-resonance excitation (1.96 eV) with the A exciton, whereas the Raman features of MoS₂ and Si overlap with the PL peak of the A exciton, particularly below 100 K, hampering to distinguish the A exciton feature (see Supplementary Information Fig. S3). The helicity parameter (P) of A exciton is approximately 80%, where $P = (I_{\sigma^-} - I_{\sigma^+}) / (I_{\sigma^-} + I_{\sigma^+})$, and I_{σ^-} and I_{σ^+} are the intensities of the right-handed (σ^-) and left-handed (σ^+) circularly polarized PL. However, the defect emission is unpolarized upon excitation at 1.96 and 2.41 eV because off-resonance excitation results in the simultaneous occurrence of optical transitions in both the +K and -K valleys.²

The interaction of the magnetic moment with the magnetic field lifts the spin states, leading to splitting of the energy level. The defect states exhibit an unambiguous momentum dependence in the vicinity of the +K and -K valleys, implying the feasibility of controlling the defect pseudospin through the Zeeman effect under an external magnetic field. The exfoliated monolayer MoS₂ are used as the control sample to study the valley Zeeman splitting of A excitons. Figure 3a and 3b show the normalized polarization-resolved PL spectra of the defect-localized excitons and A excitons at selected magnetic fields. At zero magnetic field (middle), the right-handed (+K valley, red curve, σ^-) and left-handed (-K valley, blue curve, σ^+) PL emission completely overlap. However, the σ^- (σ^+) PL peak shifts to a higher energy than that of σ^+ (σ^-) at -7 T (+7 T), indicating that valley Zeeman splitting of defect states takes

place. Figure 3c shows the PL intensity difference (ΔPL) in the normalized polarization-resolved PL spectra of defect states at ± 7 T and 0 T, $\Delta PL = I(\sigma^-) - I(\sigma^+)$, where $I(\sigma^-)$ and $I(\sigma^+)$ are the σ^- and σ^+ PL intensity, respectively. The ΔPL results further clearly reveals valley Zeeman splitting. At 0 T (black curve), ΔPL is almost equal to zero, however, ΔPL exhibits opposite values symmetric about 0 T when the magnetic field is ± 7 T, with a positive (negative) value for +7 T (-7 T) below ~ 1.71 eV and an inverse trend above this value. This observation indicates that the spin DOF of defect states can be controlled by a magnetic field through the valley Zeeman effect. The “center of mass peak analysis” is used to obtain the PL peak position and valley splitting as a function of magnetic field.⁵⁷ The splitting as a function of B is shown in Fig. 3d, yielding a g -factor of -6.2 for defect excitons which is enhanced by $\sim 50\%$ as compared to that of A exciton in exfoliated monolayer MoS₂ ($g = -4.2$).

Further insights into the origin of valley Zeeman splitting can be obtained from the calculated electronic band structures of monolayer MoS₂ with and without defects. The valence band maximum (VBM) of monolayer MoS₂ without S vacancies is only comprised of the $d_{x^2-y^2}$ and d_{xy} orbitals of Mo with $m = \pm 2$ in the $\pm K$ valley, while the CBM consists of the d_{z^2} orbital of Mo with $m = 0$ (Fig. 4a); the valley magnetic moments are $\pm(m_0 / m_{v/c}^*)\mu_B$ for the $-K$ and $+K$ points, therefore, the g -factor is approximately -4.^{52, 58} However, five d -orbitals of the Mo atom contribute to the defect states and VBM in monolayer MoS₂ with V_S and V_{2S} vacancies (Fig. 4b and Supplementary Information Fig. S4), including the d_{zx} and d_{zy} orbitals ($m = \pm 1$),

the $d_{x^2-y^2}$ and d_{xy} orbitals ($m = \pm 2$) and the d_{z^2} orbital ($m = 0$), whereas the CBM is still composed of the d_{z^2} orbital. Thus, the orbital magnetic moment leads to no shift in the conduction band, but a shift in the valence band edge and defect states at the $-K$ and $+K$ points.

The splitting of defect-bound excitons can be understood as a result of the interaction of the spin, orbital and valley magnetic moments with the magnetic field, as illustrated in Fig. 5. Two degenerate but inequivalent valleys ($\pm K$ valley) are associated with each other via the time-reversal symmetry in monolayer MoS₂, giving rise to opposite valley pseudospins in the $\pm K$ valleys.³⁴ Upon excitation by 2.41 eV σ^- circularly polarized light, off-resonance excitation simultaneously occurs in both the $+K$ and $-K$ valleys (Fig. 5a), as a consequence no valley-spin polarization is observed.² Defects trap carriers in real space and provide new recombination channels. The valley lifetime (γ_1) in 2D TMDs is at least tens of nanoseconds at least,⁵⁹ however, the charge transfer (γ_2) from excited states to defect states occurs within ~ 1 ps, which is at least three orders of magnitude shorter than the valley spin lifetime.⁶⁰ Thus, excited electrons quickly relax to defect states between two bands with the same spin states (Fig. 5b). Under an out-of-plane positive magnetic field, the spin-degenerate bands are lifted. The contributions from the spin magnetic moment and orbital magnetic moment of the d_{zx} and d_{zy} orbitals are the same for the defect and valence band shifts (Fig. 5c); thus these orbitals do not contribute to the valley Zeeman splitting.^{52, 57} However, the components of the $d_{x^2-y^2}$ and d_{xy} orbitals in the defect and valence band edges are significantly different (Fig. 4b and 5c); thus these orbitals

lead to different band shifts of the defect and valence states with the same shift direction in the same valley, resulting in an optical resonance shift of $-5\mu_B B/3$ in the $-K$ valley. The V_S defect (m_d^*) and valence (m_v^*) band masses are corrected in the $-K$ and $+K$ valleys, estimated to be $3.89m_0$ and $0.53m_0$ through first-principles calculations, resulting in a valley magnetic moment of $\pm(m_0/m_{v/d}^*)\mu_B$ for the valence and defect states, where μ_B is the Bohr magneton.⁵² The effective mass of the electron in the defect band edge is over 7 times that of the hole in the valence band edge, resulting in a larger shift of the defect band compared to the valence band, which leads to a significant optical resonance shift in the $+K$ and $-K$ valleys, $\Delta E_{v(-K)} = [(m_0/m_d^*) - (m_0/m_v^*)]\mu_B B$ (Fig. 5c). Thus, the valley Zeeman splitting (ΔE) of defect states is mainly determined by the atomic orbital and valley magnetic moments, which is given by $\Delta E = -2\{5/3 - [(m_0/m_d^*) - (m_0/m_v^*)]\}\mu_B B$; thus, the calculated effective g -factor for V_S defect states is approximately -6.6, and V_{2S} defect states have a g -factor of approximately -6.3 (See Supplementary Information Fig. S4), both of which are consistent with the experimental results ($g = -6.2$). Therefore, the enhanced g -factor for defect-bound excitons originates from the increased effective electron mass of defect states and d -orbital magnetic moment, indicating that the g -factor is independent of defect density

In summary, we have demonstrated valley pseudospin of defect states in CVD-grown monolayer MoS_2 . Five d -orbitals of the Mo atom and the large effective mass of electrons in defect states lead to enhanced valley Zeeman splitting and effective g -factor. Our results are not limited to monolayer MoS_2 and can be observed in a variety of TMDs, including WSe_2 , MoSe_2 and WS_2 . These features highlight the

potential to control the spin through defects toward novel quantum information devices and quantum spintronic and valleytronic devices.³⁰⁻³³

ASSOCIATED CONTENT

Supporting Information

The Supporting Information is available free of charge on the ACS Publications website

S1: Band structures of monolayer MoS₂ with one S divacancy (V_{2S}) defect and without defect.

S2: Raman feature of monolayer MoS₂.

S3: On-resonance excitation with the A exciton|

S4: Five *d*-orbital components in the electronic band structures of monolayer MoS₂ with one V_{2S} defect.

Methods

Sample Preparation: Monolayer MoS₂ was grown by CVD using S powder (99.999%, Ourchem) and MoO₃ (99.99%, Ourchem) as sources, PTAS as a seeding promoter, pieces of a 300 nm SiO₂/Si wafer as substrates, and high-purity inert argon as the carrier gas. The temperatures for the S and MoO₃ sources were elevated from room temperature to 160 and 650 °C, respectively.

Optical Spectroscopy Measurement: The PL, Raman, and reflection signals were recorded by a Witec Alpha 300R Plus confocal Raman microscope, coupled with a 7 T superconducting magnetic field and a closed cycle optical cryostat (10 K) on an XY scanning stage. A long working distance 50× objective (Olympus NA = 0.55) was

used for the low-temperature PL and reflection measurements. Polarization-resolved PL spectra were obtained under circular polarization excitation of 4 mW at both 1.96 eV and 2.41 eV, collected by the same objective, and passed through a $1/4\lambda$ waveplate and an analyzer into a spectrometer and a CCD camera.

STEM Characterization and Image Simulation: Monolayer MoS₂ flakes were transferred onto a TEM grid from the SiO₂/Si substrates through a PMMA film. An aberration-corrected JEOL ARM-200F with a cold field emission gun and an ASCOR probe corrector at 60 kV was used for STEM-ADF imaging. The convergence semiangle of the probe was ≈ 30 mrad. STEM-ADF images were collected using a half-angle range from ≈ 85 to 280 mrad. The QSTEM package was used for image simulations by assuming an aberration-free probe and an ≈ 1 Å source size to give a probe size of ≈ 1.2 Å.

First-Principles Calculations: Fully relativistic calculations within density functional theory are employed using the Quantum-ESPRESSO package. We choose ultrasoft pseudopotentials and the generalized gradient approximation (Perdew-Burke-Ernzerhof parametrization) of the exchange correlation functional in present calculations. In the calculation, a 4×4 supercell is used. Due to Brillouin zone folding, K and -K points of the 1×1 unit cell are folded onto the K and -K points of the 4×4 supercell, respectively. A 15 Å thick vacuum layer is adopted to avoid artificial interaction because of the periodic boundary conditions. A high cutoff energy of 544 eV and a precise $4 \times 4 \times 1$ for the k-point sampling are used. The structural optimization is continued until the residual forces have converged to less than $2.6 \times$

10^{-3} eV/Å and the total energy to less than 1.4×10^{-4} eV. The spin-orbit interaction is considered for the band structure calculation. To model one V_S or double V_{2S} defect in monolayer MoS₂, one S atom or two S atoms in the same column are removed in 4×4 supercell.

AUTHOR INFORMATION

Corresponding Author

* Bo Peng: bo_peng@uestc.edu.cn

* Xiaoxu Zhao: xiaoxu_zhao@u.nus.edu

* Yingchun Cheng: iameyccheng@njtech.edu.cn

ORCID

Bo Peng: 0000-0001-9411-716X

Author contributions

B.P. developed the concept, designed the experiment. B.P., Y.Q.W., L.J.D, Z.L., Y.L. prepared the manuscript. Y.Q.W., X.L. performed the PL and Raman measurements. Y.W., Y.Y. synthesized the monolayer MoS₂. Q.L.W., W.H., Y.C.C. contributed to first-principles calculations. X.X.Z, K.P.L, S.J.P contributed to the STEM measurements. L.B., L.Z., H.P.L., H.Y.C, P.H.Z, L.B.Z. discussed the mechanism of valley Zeeman splitting.

Notes

The authors declare no competing financial interest.

ACKNOWLEDGMENTS

We acknowledge financial support from National Natural Science Foundation of China (51602040, 51872039, 51525202 and 51902098), Science and Technology

Program of Sichuan (M112018JY0025) and Scientific Research Foundation for New Teachers of UESTC (A03013023601007).

REFERENCES:

1. Schaibley, J. R.; Yu, H.; Clark, G.; Rivera, P.; Ross, J. S.; Seyler, K. L.; Yao, W.; Xu, X., Valleytronics in 2D Materials. *Nat. Rev. Mater.* **2016**, *1*, 16055.
2. Mak, K. F.; He, K.; Shan, J.; Heinz, T. F., Control of Valley Polarization in Monolayer MoS₂ by Optical Helicity. *Nat. Nanotechnol.* **2012**, *7*, 494-498.
3. Zeng, H.; Dai, J.; Yao, W.; Xiao, D.; Cui, X., Valley Polarization in MoS₂ Monolayers by Optical Pumping. *Nat. Nanotechnol.* **2012**, *7*, 490-493.
4. Peng, B.; Li, Q.; Liang, X.; Song, P.; Li, J.; He, K.; Fu, D.; Li, Y.; Shen, C.; Wang, H., *et al.*, Valley Polarization of Triions and Magnetoresistance in Heterostructures of MoS₂ and Yttrium Iron Garnet. *ACS Nano* **2017**, *11*, 12257-12265.
5. Aharonovich, I.; Greentree, A. D.; Prawer, S., Diamond Photonics. *Nat. Photonics* **2011**, *5*, 397-405.
6. Gao, W. B.; Fallahi, P.; Togan, E.; Miguel-Sanchez, J.; Imamoglu, A., Observation of Entanglement between a Quantum Dot Spin and a Single Photon. *Nature* **2012**, *491*, 426-430.
7. Zhang, Z.; Zou, X.; Crespi, V. H.; Yakobson, B. I., Intrinsic Magnetism of Grain Boundaries in Two-Dimensional Metal Dichalcogenides. *ACS Nano* **2013**, *7*, 10475-10481.
8. Zhang, J.; Soon, J. M.; Loh, K. P.; Yin, J.; Ding, J.; Sullivan, M. B.; Wu, P., Magnetic Molybdenum Disulfide Nanosheet Films. *Nano Lett.* **2007**, *7*, 2370-2376.

9. Yang, Z.; Gao, D.; Zhang, J.; Xu, Q.; Shi, S.; Tao, K.; Xue, D., Realization of High Curie Temperature Ferromagnetism in Atomically Thin MoS₂ and WS₂ Nanosheets with Uniform and Flower-Like Morphology. *Nanoscale* **2015**, *7*, 650-658.
10. Huo, N.; Li, Y.; Kang, J.; Li, R.; Xia, Q.; Li, J., Edge-States Ferromagnetism of WS₂ Nanosheets. *Appl. Phys. Lett.* **2014**, *104*, 202406.
11. Mathew, S.; Gopinadhan, K.; Chan, T. K.; Yu, X. J.; Zhan, D.; Cao, L.; Rusydi, A.; Breese, M. B. H.; Dhar, S.; Shen, Z. X., *et al.*, Magnetism in MoS₂ Induced by Proton Irradiation. *Appl. Phys. Lett.* **2012**, *101*, 102103.
12. Yue, Q.; Chang, S.; Qin, S.; Li, J., Functionalization of Monolayer MoS₂ by Substitutional Doping: a First-Principles Study. *Phys. Lett. A.* **2013**, *377*, 1362-1367.
13. Ramasubramaniam, A.; Naveh, D., Mn-Doped Monolayer MoS₂: An Atomically Thin Dilute Magnetic Semiconductor. *Phys. Rev. B.* **2013**, *87*, 195201.
14. Cheng, Y. C.; Zhu, Z. Y.; Mi, W. B.; Guo, Z. B.; Schwingenschlögl, U., Prediction of Two-Dimensional Diluted Magnetic Semiconductors: Doped Monolayer MoS₂ Systems. *Phys. Rev. B.* **2013**, *87*, 100401.
15. Lin, Z.; Carvalho, B. R.; Kahn, E.; Lv, R.; Rao, R.; Terrones, H.; Pimenta, M. A.; Terrones, M., Defect Engineering of Two-Dimensional Transition Metal Dichalcogenides. *2D Mater.* **2016**, *3*, 022002.
16. Zhou, J.; Lin, J.; Sims, H.; Jiang, C.; Cong, C.; Brehm, J. A.; Zhang, Z.; Niu, L.; Chen, Y.; Zhou, Y., *et al.*, Synthesis of Co-Doped MoS₂ Monolayers with Enhanced Valley Splitting. *Adv. Mater.* **2020**, doi: 10.1002/adma.201906536.
17. Li, Q.; Zhao, X.; Deng, L.; Shi, Z.; Liu, S.; Wei, Q.; Zhang, L.; Cheng, Y.; Zhang,

- L.; Lu, H., *et al.*, Enhanced Valley Zeeman Splitting in Fe-Doped Monolayer MoS₂. **2020**, arXiv 3046591.
18. Chen, Y.; Xi, J.; Dumcenco, D. O.; Liu, Z.; Suenaga, K.; Wang, D.; Shuai, Z.; Huang, Y.-S.; Xie, L., Tunable Band Gap Photoluminescence from Atomically Thin Transition-Metal Dichalcogenide Alloys. *ACS Nano* **2013**, *7*, 4610-4616.
19. Schuler, B.; Qiu, D. Y.; Refaely-Abramson, S.; Kastl, C.; Chen, C. T.; Barja, S.; Koch, R. J.; Ogletree, D. F.; Aloni, S.; Schwartzberg, A. M., *et al.*, Large Spin-Orbit Splitting of Deep in-Gap Defect States of Engineered Sulfur Vacancies in Monolayer WS₂. *Phys. Rev. Lett.* **2019**, *123*, 076801.
20. Tongay, S.; Suh, J.; Ataca, C.; Fan, W.; Luce, A.; Kang, J. S.; Liu, J.; Ko, C.; Raghunathan, R.; Zhou, J., *et al.*, Defects Activated Photoluminescence in Two-Dimensional Semiconductors: Interplay between Bound, Charged, and Free Excitons. *Sci. Rep.* **2013**, *3*, 2657.
21. Mizuochi, N.; Makino, T.; Kato, H.; Takeuchi, D.; Ogura, M.; Okushi, H.; Nothaft, M.; Neumann, P.; Gali, A.; Jelezko, F., *et al.*, Electrically Driven Single-Photon Source at Room Temperature in Diamond. *Nat. Photonics* **2012**, *6*, 299-303.
22. Aharonovich, I.; Castelletto, S.; Simpson, D. A.; Su, C. H.; Greentree, A. D.; Prawer, S., Diamond-Based Single-Photon Emitters. *Rep. Prog. Phys.* **2011**, *74*, 076501.
23. Chen, D.; Mu, Z.; Zhou, Y.; Fröch, J. E.; Rasmit, A.; Diederichs, C.; Zheludev, N.; Aharonovich, I.; Gao, W.-b., Optical Gating of Resonance Fluorescence from a Single

- Germanium Vacancy Color Center in Diamond. *Phys. Rev. Lett.* **2019**, *123*, 033602.
24. Christle, D. J.; Falk, A. L.; Andrich, P.; Klimov, P. V.; Hassan, J. U.; Son, Nguyen T.; Janzén, E.; Ohshima, T.; Awschalom, D. D., Isolated Electron Spins in Silicon Carbide with Millisecond Coherence Times. *Nat. Mater.* **2014**, *14*, 160.
25. Zhou, Y.; Wang, Z.; Rasmita, A.; Kim, S.; Berhane, A.; Bodrog, Z.; Adamo, G.; Gali, A.; Aharonovich, I.; Gao, W.-b., Room Temperature Solid-State Quantum Emitters in the Telecom Range. *Sci. Adv.* **2018**, *4*, eaar3580.
26. Branny, A.; Kumar, S.; Proux, R.; Gerardot, B. D., Deterministic Strain-Induced Arrays of Quantum Emitters in a Two-Dimensional Semiconductor. *Nat. Commun.* **2017**, *8*, 15053.
27. Palacios-Berraquero, C.; Kara, D. M.; Montblanch, A. R. P.; Barbone, M.; Latawiec, P.; Yoon, D.; Ott, A. K.; Loncar, M.; Ferrari, A. C.; Atatüre, M., Large-Scale Quantum-Emitter Arrays in Atomically Thin Semiconductors. *Nat. Commun.* **2017**, *8*, 15093.
28. Tran, T. T.; Bray, K.; Ford, M. J.; Toth, M.; Aharonovich, I., Quantum Emission from Hexagonal Boron Nitride Monolayers. *Nat. Nanotechnol.* **2015**, *11*, 37.
29. Exarhos, A. L.; Hopper, D. A.; Patel, R. N.; Doherty, M. W.; Bassett, L. C., Magnetic-Field-Dependent Quantum Emission in Hexagonal Boron Nitride at Room Temperature. *Nat. Commun.* **2019**, *10*, 222.
30. Srivastava, A.; Sidler, M.; Allain, A. V.; Lembke, D. S.; Kis, A.; Imamoğlu, A., Optically Active Quantum Dots in Monolayer WSe₂. *Nat. Nanotechnol.* **2015**, *10*, 491-496.

31. Koperski, M.; Nogajewski, K.; Arora, A.; Cherkez, V.; Mallet, P.; Veuillen, J. Y.; Marcus, J.; Kossacki, P.; Potemski, M., Single Photon Emitters in Exfoliated WSe₂ Structures. *Nat. Nanotechnol.* **2015**, *10*, 503-506.
32. He, Y.-M.; Clark, G.; Schaibley, R. J.; He, Y.; Chen, C-M; Wei, Y. J.; Ding, X.; Zhang, Q.; Yao, W.; Xu, X., *et al.*, Single Quantum Emitters in Monolayer Semiconductors. *Nat. Nanotechnol.* **2015**, *10*, 497-502.
33. Chakraborty, C.; Kinnischtzke, L.; Goodfellow, K. M.; Beams, R.; Vamivakas, A. N., Voltage-Controlled Quantum Light from an Atomically Thin Semiconductor. *Nat. Nanotechnol.* **2015**, *10*, 507-511.
34. Xiao, D.; Liu, G.; Feng, W.; Xu, X.; Yao, W., Coupled Spin and Valley Physics in Monolayers of MoS₂ and Other Group-VI Dichalcogenides. *Phys. Rev. Lett.* **2012**, *108*, 196802.
35. Refaely-Abramson, S.; Qiu, D. Y.; Louie, S. G.; Neaton, J. B., Defect-Induced Modification of Low-Lying Excitons and Valley Selectivity in Monolayer Transition Metal Dichalcogenides. *Phys. Rev. Lett.* **2018**, *121*, 167402.
36. Wang, Q.; Ge, S.; Li, X.; Qiu, J.; Ji, Y.; Feng, J.; Sun, D., Valley Carrier Dynamics in Monolayer Molybdenum Disulfide from Helicity-Resolved Ultrafast Pump–Probe Spectroscopy. *ACS Nano* **2013**, *7*, 11087-11093.
37. Neumann, A.; Lindlau, J.; Colombier, L.; Nutz, M.; Najmaei, S.; Lou, J.; Mohite, A. D.; Yamaguchi, H.; Högele, A., Opto-Valleytronic Imaging of Atomically Thin Semiconductors. *Nat. Nanotechnol.* **2017**, *12*, 329-334.
38. Chow, P. K.; Jacobs-Gedrim, R. B.; Gao, J.; Lu, T.-M.; Yu, B.; Terrones, H.;

- Korotkar, N., Defect-Induced Photoluminescence in Monolayer Semiconducting Transition Metal Dichalcogenides. *ACS Nano* **2015**, *9*, 1520-1527.
39. Chakraborty, C.; Goodfellow, K. M.; Nick Vamivakas, A., Localized Emission from Defects in MoSe₂ Layers. *Opt. Mater. Express* **2016**, *6*, 2081-2087.
40. Hsu, W.-T.; Chen, Y.-L.; Chen, C.-H.; Liu, P.-S.; Hou, T.-H.; Li, L.-J.; Chang, W.-H., Optically Initialized Robust Valley-Polarized Holes in Monolayer WSe₂. *Nat. Commun.* **2015**, *6*, 8963.
41. Wu, Z.; Zhao, W.; Jiang, J.; Zheng, T.; You, Y.; Lu, J.; Ni, Z., Defect Activated Photoluminescence in WSe₂ Monolayer. *J. Phys. Chem. C* **2017**, *121*, 12294-12299.
42. Cheng, Y. C.; Zhang, Q. Y.; Schwingenschlögl, U., Valley Polarization in Magnetically Doped Single-Layer Transition-Metal Dichalcogenides. *Phys. Rev. B.* **2014**, *89*, 155429.
43. Zhang, Q.; Yang, S. A.; Mi, W.; Cheng, Y.; Schwingenschlögl, U., Large Spin-Valley Polarization in Monolayer MoTe₂ on Top of Euo(111). *Adv. Mater.* **2016**, *28*, 959-966.
44. Zhou, W.; Zou, X.; Najmaei, S.; Liu, Z.; Shi, Y.; Kong, J.; Lou, J.; Ajayan, P. M.; Yakobson, B. I.; Idrobo, J.-C., Intrinsic Structural Defects in Monolayer Molybdenum Disulfide. *Nano Lett.* **2013**, *13*, 2615-2622.
45. Hong, J.; Hu, Z.; Probert, M.; Li, K.; Lv, D.; Yang, X.; Gu, L.; Mao, N.; Feng, Q.; Xie, L., *et al.*, Exploring Atomic Defects in Molybdenum Disulphide Monolayers. *Nat. Commun.* **2015**, *6*, 6293.
46. Wan, Y.; Zhang, H.; Zhang, K.; Wang, Y.; Sheng, B.; Wang, X.; Dai, L.,

Large-Scale Synthesis and Systematic Photoluminescence Properties of Monolayer MoS₂ on Fused Silica. *ACS Appl. Mater. Interfaces* **2016**, *8*, 18570-18576.

47. Wang, Y.; Cong, C.; Qiu, C.; Yu, T., Raman Spectroscopy Study of Lattice Vibration and Crystallographic Orientation of Monolayer MoS₂ under Uniaxial Strain. *Small* **2013**, *9*, 2857-2861.

48. Peng, B.; Li, J.; Li, Q.; Li, Y.; Zhu, H.; Zhang, L.; Wang, X.; Bi, L.; Lu, H.; Xie, J., *et al.*, Bose-Einstein Oscillators and the Excitation Mechanism of Free Excitons in 2D Layered Organic-Inorganic Perovskites. *RSC Adv.* **2017**, *7*, 18366-18373.

49. Sidler, M.; Back, P.; Cotlet, O.; Srivastava, A.; Fink, T.; Kroner, M.; Demler, E.; Imamoglu, A., Fermi Polaron-Polaritons in Charge-Tunable Atomically Thin Semiconductors. *Nat. Phys.* **2016**, *13*, 255.

50. Mak, K. F.; He, K.; Lee, C.; Lee, G. H.; Hone, J.; Heinz, T. F.; Shan, J., Tightly Bound Trions in Monolayer MoS₂. *Nat Mater* **2013**, *12*, 207-211.

51. Ye, Z.; Cao, T.; O'Brien, K.; Zhu, H.; Yin, X.; Wang, Y.; Louie, S. G.; Zhang, X., Probing Excitonic Dark States in Single-Layer Tungsten Disulphide. *Nature* **2014**, *513*, 214-218.

52. Wang, Z.; Mak, K. F.; Shan, J., Strongly Interaction-Enhanced Valley Magnetic Response in Monolayer WSe₂. *Phys. Rev. Lett.* **2018**, *120*, 066402.

53. Kc, S.; Longo, R. C.; Addou, R.; Wallace, R. M.; Cho, K., Impact of Intrinsic Atomic Defects on the Electronic Structure of MoS₂ monolayers. *Nanotechnology* **2014**, *25*, 375703.

54. Najmaei, S.; Yuan, J.; Zhang, J.; Ajayan, P.; Lou, J., Synthesis and Defect

- Investigation of Two-Dimensional Molybdenum Disulfide Atomic Layers. *Acc. Chem. Res.* **2015**, *48*, 31-40.
55. Zhang, C.; Johnson, A.; Hsu, C.-L.; Li, L.-J.; Shih, C.-K., Direct Imaging of Band Profile in Single Layer MoS₂ on Graphite: Quasiparticle Energy Gap, Metallic Edge States, and Edge Band Bending. *Nano Lett.* **2014**, *14*, 2443-2447.
56. Hill, H. M.; Rigosi, A. F.; Roquelet, C.; Chernikov, A.; Berkelbach, T. C.; Reichman, D. R.; Hybertsen, M. S.; Brus, L. E.; Heinz, T. F., Observation of Excitonic Rydberg States in Monolayer MoS₂ and WS₂ by Photoluminescence Excitation Spectroscopy. *Nano Lett.* **2015**, *15*, 2992-2997.
57. Aivazian, G.; Gong, Z.; Jones, A. M.; Chu, R.-L.; Yan, J.; Mandrus, D. G.; Zhang, C.; Cobden, D.; Yao, W.; Xu, X., Magnetic Control of Valley Pseudospin in Monolayer WSe₂. *Nat. Phys.* **2015**, *11*, 148-152.
58. Kang, J.; Tongay, S.; Zhou, J.; Li, J.; Wu, J., Band Offsets and Heterostructures of Two-Dimensional Semiconductors. *Appl. Phys. Lett.* **2013**, *102*, 012111.
59. Kim, J.; Jin, C.; Chen, B.; Cai, H.; Zhao, T.; Lee, P.; Kahn, S.; Watanabe, K.; Taniguchi, T.; Tongay, S., *et al.*, Observation of Ultralong Valley Lifetime in WSe₂/MoS₂ Heterostructures. *Sci. Adv.* **2017**, *3*, e1700518.
60. Peng, B.; Yu, G.; Liu, X.; Liu, B.; Liang, X.; Bi, L.; Deng, L.; Sum, T. C.; Loh, K. P., Ultrafast Charge Transfer in MoS₂/WSe₂ *p-n* Heterojunction. *2D Mater.* **2016**, *3*, 025020.

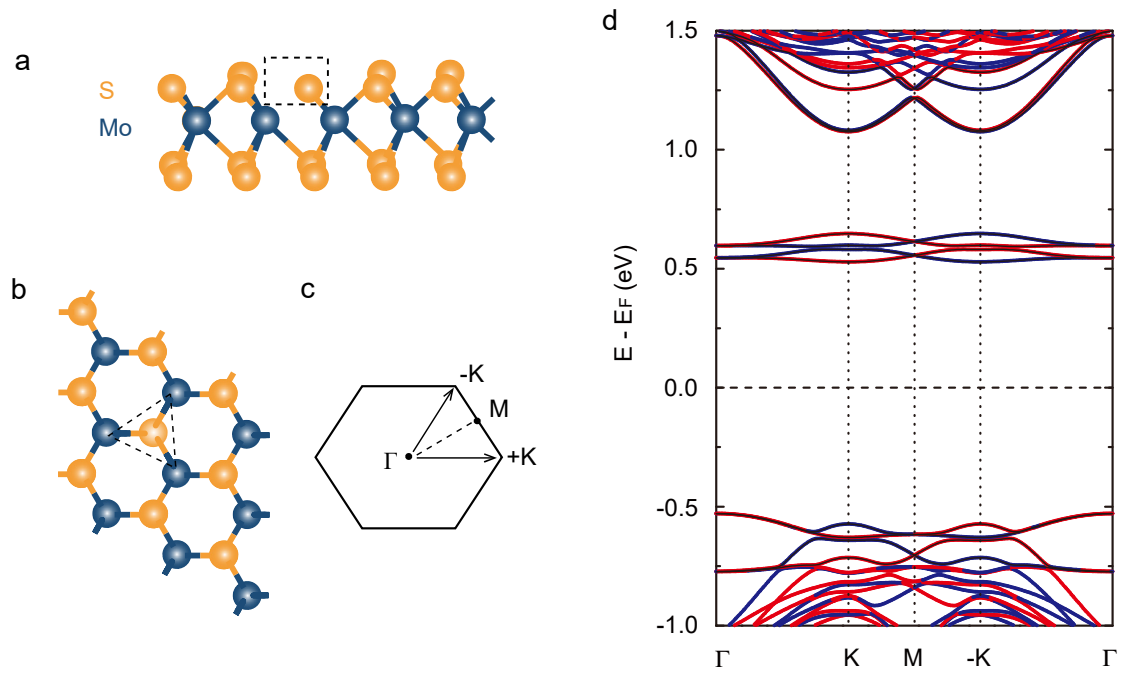


Fig. 1. Band structures of monolayer MoS₂ with one V_S defect. (a, b) Side and top views of the monolayer 1H-MoS₂ structure with one V_S defect. **(c)** Brillouin zone of monolayer MoS₂. **(d)** Electronic band structure of monolayer MoS₂ with one V_S defect. Blue (red) curves represent spin-up (spin-down) states in the +K (-K) valley.

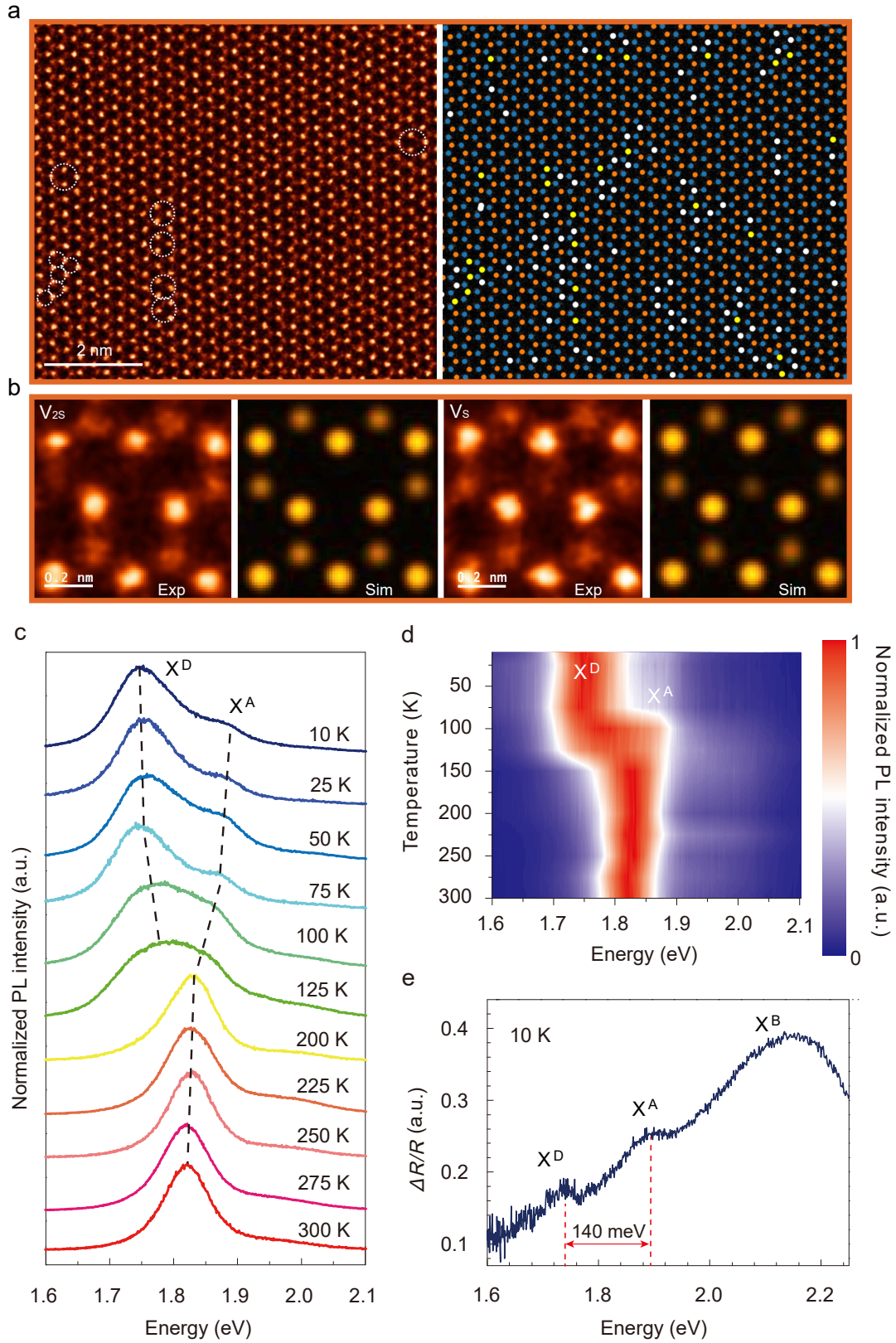


Fig. 2. Strong defect emission from V_S and V_{2S} defects in monolayer MoS₂. (a)

Atomic-resolution STEM-ADF images of 1H-MoS₂ monolayer with V_S and V_{2S}

(white dashed circle) defects. Corresponding atomic mode showing the distribution of V_S and V_{2S} defect, which are depicted as white and yellow spheres. **(b)** Enlarged STEM-ADF image and corresponding simulated image revealing V_S and V_{2S} defect. The scale bare in b is 0.2 nm. **(c, d)** PL spectra of monolayer MoS_2 and corresponding two dimensional image as a function of temperature upon excitation by 2.41 eV light. A strong defect emission (X^D) accompanied with A exciton emission (X^A) is observed below 100 K. **(e)** Absorption spectra of the corresponding monolayer MoS_2 at 10 K, indicating an unambiguous defect absorption features, in addition to the A exciton and B exciton (X^B) features.

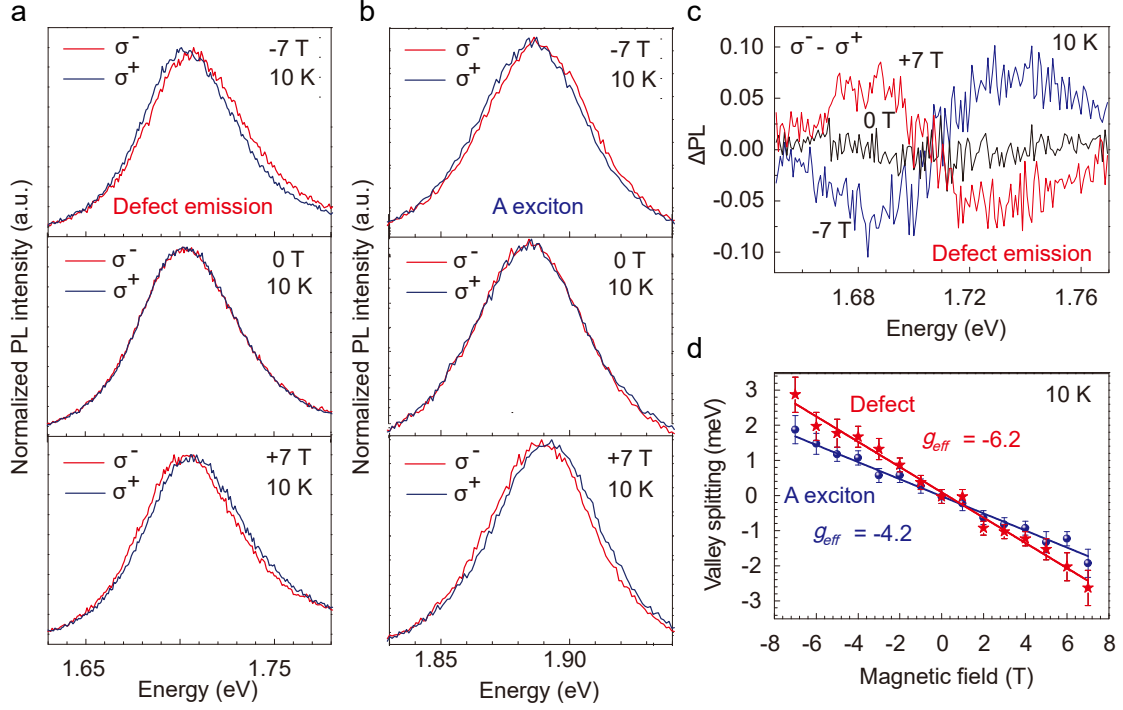


Fig. 3. Valley Zeeman splitting of defect emission. (a, b) Normalized raw polarization-resolved PL spectra of defect-localized excitons and A exciton (exfoliated MoS₂) in magnetic field of 0 and ± 7 T at 10 K. The σ^- and σ^+ PL spectra completely overlap at 0 T, but they split at +7 T and -7 T with opposite shift direction. (c) Difference in the normalized σ^- and σ^+ PL components at 0 and ± 7 T, which show no difference at 0 T but striking opposite trends at ± 7 T, strongly manifesting that valley Zeeman splitting of defect states occurs. (d) Valley splitting as a function of the magnetic field at 10 K, giving an effective g-factor of -6.2 (defect-localized excitons) and -4.2 (A excitons). The PL peak position and valley splittings as a function of magnetic field were obtained through “center of mass peak analysis” (Ref. 48).

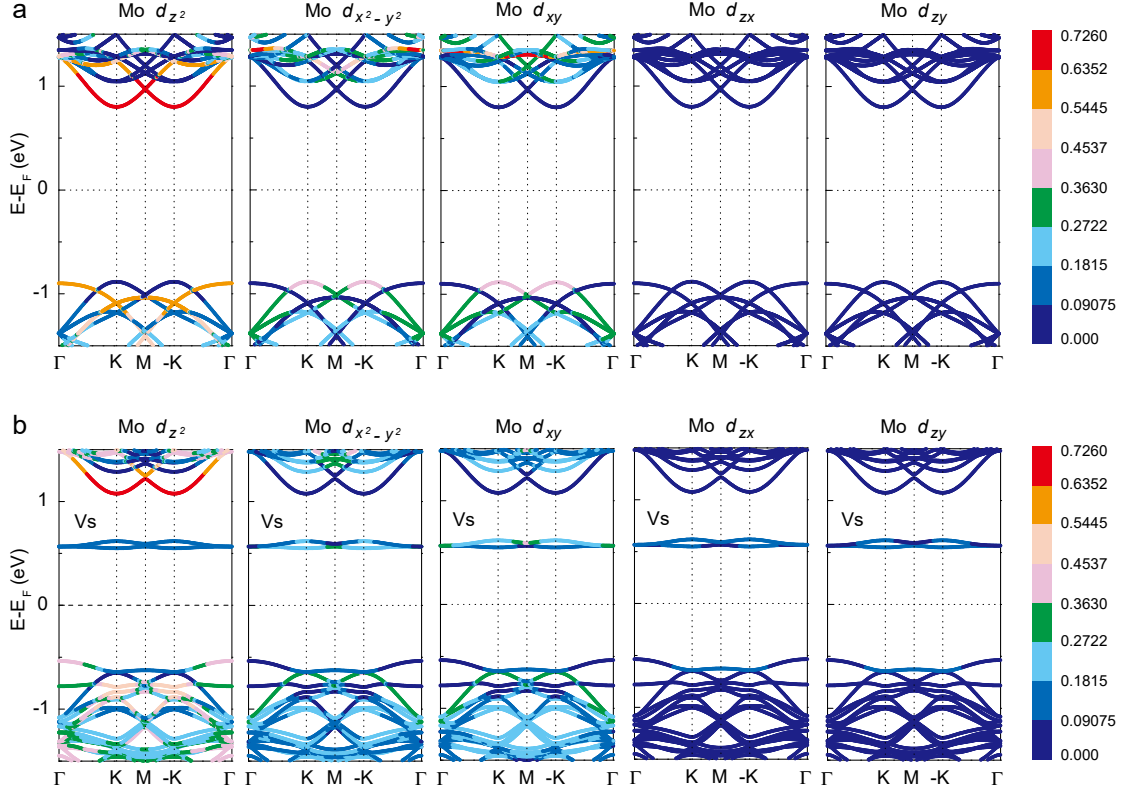


Fig. 4. Origin of valley Zeeman splitting of defect states. (a, b) Five d -orbital components in the electronic band structures of monolayer MoS₂ without defects **(a)** and with one V_S defect **(b)**. The conduction band edges of monolayer MoS₂ with and without defects consist of the d_{z^2} ($m=0$) orbitals. The valence band edges of monolayer MoS₂ without defect in the vicinity of the $\pm K$ valleys are mainly composed of the $d_{x^2-y^2}$ ($m=\pm 2$) and d_{xy} ($m=\pm 2$) orbitals. However, the valence and defect band edges monolayer MoS₂ with one single S vacancy are composed of all five d -orbitals.

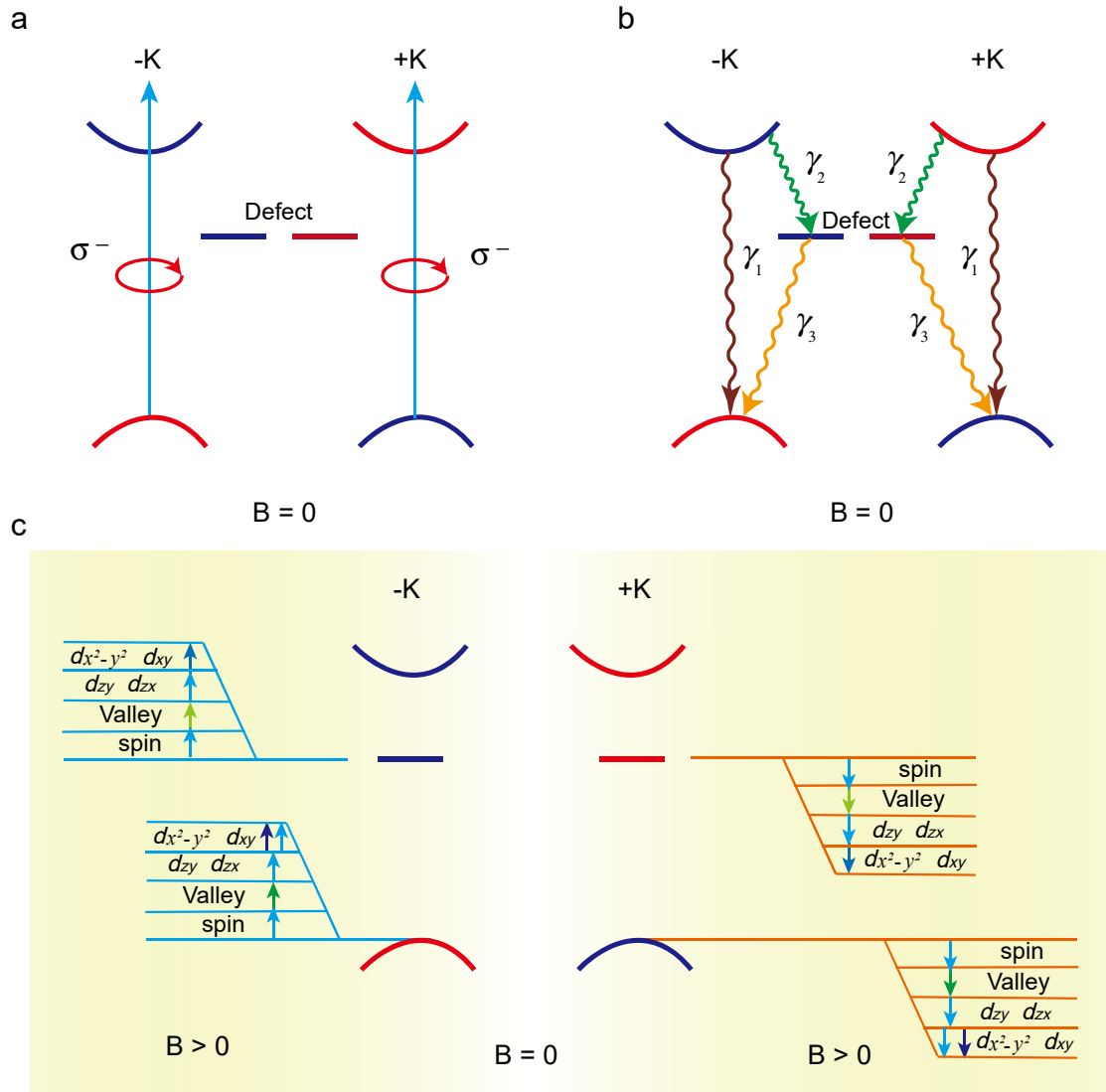


Fig. 5. Valley Zeeman splitting of defect-bound excitons under a magnetic field.

(a) Off-resonance excitation by right-hand polarized light at 2.41 eV simultaneously occur in the $-K$ and $+K$ valleys. **(b)** Corresponding charge carrier relaxation process upon off-resonance excitation. **(c)** Valley Zeeman splitting under a magnetic field as a result of contributions from the spin magnetic moment, valley magnetic moment and d -orbital magnetic moment of the band edge of defect and valence states.